PHOTONICS Research

# Photonic topological transition in dimerized chains with the joint modulation of near-field and far-field couplings

Caifu Fan,[1] Xi Shi,[2,4] Feng Wu,[3] Yunhui Li,[1] Haitao Jiang,[1] Yong Sun,[1,5] and Hong Chen[1]

[1]MOE Key Laboratory of Advanced Micro-Structured Materials, School of Physics Science and Engineering, Tongji University, Shanghai 200092, China
[2]Department of Physics, Shanghai Normal University, Shanghai 200234, China
[3]School of Optoelectronic Engineering, Guangdong Polytechnic Normal University, Guangzhou 510665, China
[4]e-mail: xishi@shnu.edu.cn
[5]e-mail: yongsun@tongji.edu.cn

Received 24 August 2021; revised 18 October 2021; accepted 31 October 2021; posted 2 November 2021 (Doc. ID 441278); published 9 December 2021

**Topological systems containing near-field or far-field couplings between unit cells have been widely investigated in quantum and classic systems. Their band structures are well explained with theories based on tight-binding or multiple scattering formalism. However, characteristics of the topology of the bulk bands based on the joint modulation of near-field and far-field couplings are rarely studied. Such hybrid systems are hardly realized in real systems and cannot be described by neither tight-binding nor multiple scattering theories. Here, we propose a hybrid-coupling photonic topological insulator based on a quasi-1D dimerized chain with the coexistence of near-field coupling within the unit cell and far-field coupling among all sites. Both theoretical and experimental results show that topological transition is realized by introducing near-field coupling for given far-field coupling conditions. In addition to closing and reopening the bandgap, the change in near-field coupling modulates the effective mass of photonics in the upper band from positive to negative, leading to an indirect bandgap, which cannot be achieved in conventional dimerized chains with either far-field or near-field coupling only.** 

https://doi.org/10.1364/PRJ.441278

## 1. INTRODUCTION

Inspired by the conception of topological insulators in electron systems [1–4], topological photonics provide a new platform to demonstrate the exotic electromagnetic (EM) wave transportation phenomena, such as reflection-free one-way edge modes [5], non-Hermitian topological light steering [6], and topological multifrequency trapping [7,8]. As a growing research field in recent years, massive efforts have been devoted to uncovering the untrivial topological properties [9–18]. The progress in topological photonics covers a broad spectrum, such as high-order topology [19–22], non-Hermitian topology [23,24], nonlinear topological interface state [25], and Floquet topological insulators [26]. Because of the topological protection mechanism, it is demonstrated that topological edge modes are robust against the imperfections of the materials and thus can be applied to unidirectional transmission [5,27,28], topologically protected optical delay line [29–31], and defect-immune information transmission [32]. Especially, 1D topological photonic systems have attracted a lot of attention due to their clear physical concept and easy fabrication [33–42]. According to the different coupling mechanism in photonic topological insulators (PTIs), one can classified them into two categories: near-field-coupling PTIs or far-field-coupling PTIs. In near-field-coupling PTIs, for instance, the Su–Schrieffer–Heeger (SSH) model describes topology in dimerized 1D structures with alternating near-field evanescent couplings [43–45]. In far-field-coupling PTIs, for example, photonic crystals with periodic wavelength-scaled structures give topological band inversion because of the far-field couplings mechanism [18,46,47]. Although the coupling mechanism is different, their systematic Hamiltonians are Hermitian. Bloch bulk bands thus can be described by tight-binding or multiple scattering theories to classify topological bands.

Recently, hybrid-coupling systems containing both near-field couplings and far-field couplings have attracted ongoing interest. These photonic structures introduced more degrees of freedom to modulate the EM wave in new ways, such as bound states in the continuum [48,49] and topological Fano resonances [50,51]. However, the topologies of the bulk bands of hybrid-coupling PTIs are rarely studied because the band

structures of hybrid-coupling systems cannot be derived using either tight-binding or multiple scattering theory. On the other hand, it is difficult to have a photonic structure in which near-field coupling and far-field coupling can be independently adjusted.

In this paper, we propose a model of hybrid-coupling PTIs based on a special quasi-1D dimerized chain with the coexistence of near-field coupling within the unit cell and far-field coupling among all sites. As a new controllable degree of freedom, the effect of the intracell near-field coupling on the band structure is investigated using the Bloch band theory based on temporal coupled-mode theory and transfer matrix method. A topological transition of such hybrid-coupling PTIs is achieved. It is noted that the joint modulation of both types of coupling makes switching the band topology more flexible, compared to that in the ordinary 1D systems with either far-field or near-field coupling. In detail, the propagating phase (far-field coupling) and the near-field coupling between two resonant scatters in the same unit cell can be independently adjusted by the distance along the backbone waveguide and their mutual inductance, and the band topologies of the system, which are characterized with Zak phases, can be controlled by these two variables. The interface mode in the heterostructure composed of a far-field-coupling PTI and a hybrid-coupling PTI with distinguished band topology is demonstrated experimentally by measuring the reflection and the field distribution. Moreover, the change in near-field coupling in this hybrid-coupling PTI modulates the effective mass of photonics in the interested band from positive to zero (flat band) to negative, and finally results in an indirect bandgap, which is impossible in ordinary dimerized chains. We believe our results pave the way to understand the unique role of hybrid coupling in band topology, and may find applications in compact wave absorbers, filters, and topological photonic devices.

## 2. TOPOLOGICAL PHASE TRANSITION IN THE 1D DIMERIZED FAR-FIELD-COUPLING PTIS

We start with a simple model to describe a dimerized 1D chain with far-field coupling only. The scheme of the chain is shown in Fig. 1(a). $A_n$ and $B_n$ represent two locally resonant scatters in the $n$th unit cell. They have the same resonance frequency $f_0$, and are coupled to the backbone waveguide at the same coupling rate $\gamma$. The scattering waves of the resonant scatters are radiated into the single-mode backbone waveguide; thus, the far-field coupling among the scatters is achieved through the backbone waveguide in indirect manners. In contrast, the near-field coupling originates from the direct superposition of the evanescent waves from the adjacent scatters. A parameter $\Delta = d/L$ is introduced to describe the dimerization, where $d$ is the distance between $A_n$ and $B_n$ along the waveguide, and $L$ is the period of the dimerized chain.

$A_n$ and $B_n$ in a compound unit cell can couple with all the other resonant scatters through the propagating waves in the backbone waveguide. For the $n$th compound unit cell shown in Fig. 1(b), the dynamic equations for two resonance modes ($\tilde{a}_n = a_n e^{i\omega t}$ and $\tilde{b}_n = b_n e^{i\omega t}$) at $A_n$ and $B_n$ can be written as [52,53]

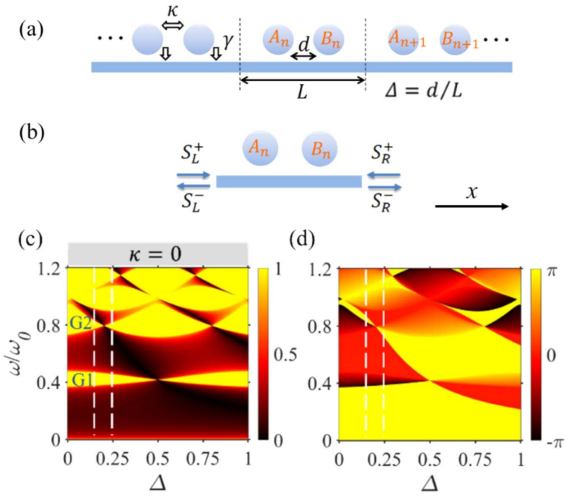


**Fig. 1.** (a) 1D dimerized chain with the unit cell length $L$ and the distance $d$ between two sites $A_n$ and $B_n$. $\Delta = d/L$ is the dimerized parameter. Two sites $A_n$ and $B_n$ are both coupled to the backbone waveguide at the same coupling rate $\gamma$, and they are directly coupled to each other through near field at a coupling rate $\kappa$. (b) Schematic of the unit cell excited by the left and right incident EM waves noted as $S_L^+$ and $S_R^+$. The output EM waves from two sides are noted as $S_L^-$ and $S_R^-$. (c) Reflectivity and (d) reflection phase for a semi-infinite 1D chain modulated by the dimerized parameter $\Delta$ with the vanished near-field coupling ($\kappa = 0$). The first and second band gaps are noted as G1 and G2 in (c). The second and third pass bands are inversed for the 1D dimerized chain with two different dimerized parameters $\Delta = 0.165$ and $\Delta = 0.25$ (denoted by the white dashed lines). The reflection phases of these two cases for the second band gap have different signs.

$$\dot{\tilde{a}}_n = (i\omega_0 - \gamma)\tilde{a}_n + C\tilde{b}_n + i\sqrt{\gamma}e^{-ikL(1-\Delta)/2}\tilde{S}_L^+ + i\sqrt{\gamma}e^{-ikL(1+\Delta)/2}\tilde{S}_R^+, \quad (1)$$

$$\dot{\tilde{b}}_n = (i\omega_0 - \gamma)\tilde{b}_n + C\tilde{a}_n + i\sqrt{\gamma}e^{-ikL(1+\Delta)/2}\tilde{S}_L^+ + i\sqrt{\gamma}e^{-ikL(1-\Delta)/2}\tilde{S}_R^+, \quad (2)$$

where $C = -\gamma e^{-ik\Delta L}$ ($k = \omega/c$ is the propagation constant of the backbone waveguide) indicates the far-field coupling between two resonance modes, and $\tilde{S}_L^+ = S_L^+ e^{i\omega t}$ and $\tilde{S}_R^+ = S_R^+ e^{i\omega t}$ denote the incoming waves from the left and right sides, as shown in Fig. 1(b). $\omega_0 = 2\pi f_0$ is the resonance angular frequency. Since the unit cell is reciprocal and mirror-symmetrical, the output waves $S_L^-$ and $S_R^-$ at two sides are related to $S_L^+$ and $S_R^+$ by the scattering matrix

$$\begin{pmatrix} S_L^- \\ S_R^- \end{pmatrix} = \begin{pmatrix} t & r \\ r & t \end{pmatrix} \begin{pmatrix} S_R^+ \\ S_L^+ \end{pmatrix}. \quad (3)$$

The transfer matrix of a unit cell in the EM system can be obtained from Eq. (3) by rearranging the incidence waves and outgoing waves as

$$\begin{pmatrix} S_L^+ \\ S_L^- \end{pmatrix} = \begin{pmatrix} \frac{1}{t} & -\frac{r_R}{t} \\ \frac{r_L}{t} & \frac{t^2 - r_L r_R}{t} \end{pmatrix} \begin{pmatrix} S_R^- \\ S_R^+ \end{pmatrix} = T \begin{pmatrix} S_R^- \\ S_R^+ \end{pmatrix}. \quad (4)$$

We suppose $S_R^+ = 0$. The output wave at the right side in the waveguide is the superposition of the directly transmitted

EM waves $S_L^+ e^{-ikL}$, and the scattering waves from the resonators $i\sqrt{\gamma}e^{-ikL(1+\Delta)/2}a_n$ and $i\sqrt{\gamma}e^{-ikL(1-\Delta)/2}b_n$. The reflection wave at the left side is the superposition of the scattering waves from two sites. Hence, the transmission and reflection coefficients for the unit cell can be obtained by

$$t = e^{-ikL} + [i\sqrt{\gamma}e^{-ikL(1+\Delta)/2}a_n + i\sqrt{\gamma}e^{-ikL(1-\Delta)/2}b_n]/S_L^+, \quad (5)$$

$$r = [i\sqrt{\gamma}e^{-ikL(1-\Delta)/2}a_n + i\sqrt{\gamma}e^{-ikL(1+\Delta)/2}b_n]/S_L^+. \quad (6)$$

Then, we can calculate the band structures, as well as the transmission and reflection coefficients for the 1D chains based on the scattering matrix.

The topological phase transitions are commonly accompanied by the closing and reopening of the band gaps, which correspond to the total reflection bands for a semi-infinite structure. We first calculate the reflectivity and reflection phase of a semi-infinite dimerized chain with the help of impedance boundary condition (see Appendix A), with the fitted parameters $f_0 = 5.83$ GHz, $\gamma = 4.19$ GHz, and $L = 40$ mm. The reflectivity and the reflection phase as functions of $\Delta$ and $\omega$ are shown in Figs. 1(c) and 1(d), respectively. Here, we focus on the second band gap (G2) of the 1D chain. It gradually closes and then reopens by continuously tuning the dimerized parameter from $\Delta = 0.165$ to $\Delta = 0.25$ [white dashed lines in Figs. 1(c) and 1(d)]. The topological phase transitions occur at $\Delta = 0.203$ (or $\Delta = 0.797$) at which the structure with two adjacent scatters meets the Fabry–Perot (FP) cavity conditions at the second Bragg frequency ($\omega = 0.8\omega_0$). In addition, the change of the sign of the reflection phase for this band gap also confirms the topological phase transition [47].

## 3. TOPOLOGICAL PHASE TRANSITION IN THE 1D DIMERIZED HYBRID-COUPLING PTIS

Next, we extend the multiple scattering theory into the 1D dimerized far-field coupling model with additional near-field coupling between two scatters $A_n$ and $B_n$ in the unit cell. The hybrid coupling in Eqs. (1) and (2) is rewritten as $C = -\gamma e^{-ik\Delta L} - i\kappa$, where $\kappa$ is the near-field coupling between $A_n$ and $B_n$. The calculated reflectivity as a function of $\Delta$ and $\omega$ for $\kappa = -0.044\omega_0$ and $\kappa = -0.137\omega_0$ is plotted in Figs. 2(a) and 2(c), and the corresponding reflection phase is shown in Figs. 2(b) and 2(d), respectively. If we take a specific dimerized parameter, for instance, $\Delta = 0.165$, the second band gap closes at $\kappa = -0.044\omega_0$ and reopens at $\kappa = -0.137\omega_0$ due to the joint modulation of near-field and far-field coupling. It is noticed that, in the purely far-field coupling condition [Fig. 1(c)], the symmetry inversion of reflectivity happens as $\Delta = 0.5$, which corresponds to the case of a chain with a single elementary unit cell of size $L/2$. This symmetry inversion of reflectivity breaks in the hybrid coupling conditions in Figs. 2(a) and 2(c).

To investigate in detail the modulation of topological properties in the presence of near-field coupling, the reflectivity and reflection phase are given in Fig. 3 as functions of near-field coupling $\kappa$ and $\omega$ for $\Delta = 0.165$. The near-field coupling is physically different from the far-field coupling. The far-field coupling stems from multiple scattering, which means that shifting the dimerized parameters will affect the physical

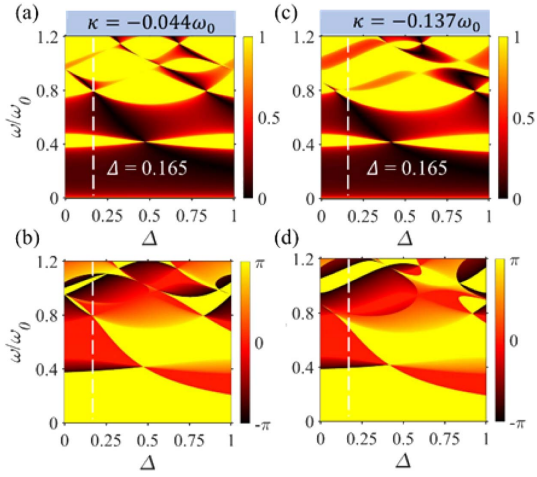


**Fig. 2.** (a) Reflectivity and (b) reflection phase of the semi-infinite 1D dimerized chain with intracell near-field coupling $\kappa = -0.044\omega_0$. Similarly, (c) and (d) are the reflectivity and reflection phase of the 1D chain with the near-field coupling $\kappa = -0.137\omega_0$. For a fixed dimerized parameter $\Delta = 0.165$ indicated by the white dashed lines in (a)–(d), the second band gap closes in (a) and reopens in (c).

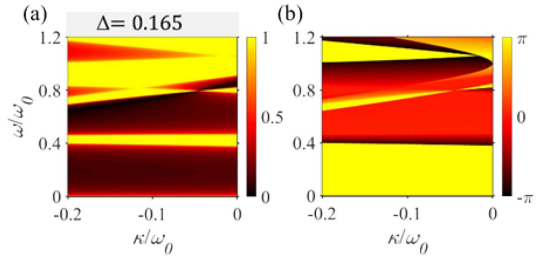


**Fig. 3.** (a) Reflectivity and (b) reflection phase of the semi-infinite 1D dimerized chain as functions of near-field coupling and frequency for a specific dimerized parameter $\Delta = 0.165$. The gradually increased near-field coupling strength leads to the band inversion for the second and third bands. The second band gap closes at $\kappa = -0.047\omega_0$.

properties for all passbands, whereas the near-field coupling modulates only limited bands near the resonant frequency of the units. The first band gap in Fig. 3(a) keeps almost unchanged as it is away from the resonance frequency and is not influenced by the near-field coupling. For the second band gap, the band inversion is observed with the increasing strength of near-field coupling. Hence, the near-field coupling, serving as a new degree of freedom, is an effective parameter to control topological properties of the dimerized 1D chain.

To fully uncover the topological properties of this hybrid coupling 1D model, we give the band structures of hybrid systems. In the condition of the Bloch boundary condition $S_R^- = e^{iqL}S_L^+$ and $S_L^- = e^{iqL}S_R^+$, the scattering matrix $S = \begin{pmatrix} t & r_L \\ r_R & t \end{pmatrix}$ in Eq. (3) can transform to

$$\left| S - \begin{pmatrix} e^{-iqL} & 0 \\ 0 & e^{iqL} \end{pmatrix} \right| = 0, \quad (7)$$

where $q$ denotes the Bloch wave vector.

The dispersion relation cannot be presented as an elegant analytical solution because of the complexity of this model. But we can numerically calculate the band structures for different near-field coupling strengths $\kappa$ with the fixed dimerized parameter of $\Delta = 0.165$, as shown in Fig. 4. We mark the first four bands and first four (or three) band gaps as B1–B4 and G1–G4 (G3), respectively. As the near-field coupling strength $|\kappa|$ increases, the bands B2 and B3 touch each other at $\kappa = -0.044\omega_0$ in Fig. 4(b), and then separate again [see Figs. 4(c)–4(f)].

We calculate the Zak phases of the first few bands to describe the topological transition quantitatively. Zak phases are initially defined as the characteristic quantity to describe the electron movement in a 1D periodic solid system [54] and then extended to a 1D photonic system with mirror symmetry to depict the topological properties of pass bands. Generally, the Zak phase can be calculated based on the original definition. First, one can find the period part $u_{n,q}$ of the Bloch wave $E_{n,q}$ that meets the relation $E_{n,q} = u_{n,q}e^{iqx}$. The Bloch wave can be obtained from the eigenvector of the transfer matrix of the entire unit cell and thus we define the Zak phase as [18]

$$\theta_n^{\mathrm{Zak}} = \int_{-\pi/L}^{\pi/L} \left[ i \int_{-L/2}^{L/2} \mathrm{d}x \varepsilon(x) u_{n,q}^*(x) \partial_q u_{n,q}(x) \right] \mathrm{d}q, \quad (8)$$

where $i\int_{-L/2}^{L/2} \mathrm{d}x \varepsilon(x) u_{n,q}^*(x) \partial_q u_{n,q}(x)$ is the Berry connection, $\varepsilon(x)$ represents the dielectric function of the transmission channel, and the EM waves propagate along the $x$ direction. For this dimerized chain, one can quantize the Zak phase at either 0 or $\pi$. However, the Zak phase is ill-defined for the case where two pass bands are crossed. This issue can be overcome by bringing in the surface bulk correspondence in the 1D system. The rigorous relation between the sign of the reflection phase in the $n$th gap and the sum of Zak phases of all the isolated bands below the band gap can be described as

$$\mathrm{sgn}[\arg(r_n)] = (-1)^n(-1)^p \exp\left( i \sum_{m=1}^{n} \theta_m^{\mathrm{Zak}} \right), \quad (9)$$

where $p$ is the number of band crossing points below the $n$th band gap.

The Zak phase of an isolated band can also be determined by identifying all zero-reflection states of the semi-infinite 1D chain (or a single unit cell). It has been demonstrated that each zero-reflection state corresponding to a singular point of zero reflection in reflection spectrum contributes $\pi$ to the Zak phase. The Zak phase of each isolated band obtained by this method is given in Fig. 4 for different $\Delta$. The singular points in the studied frequency bands originate from two different mechanisms [47]. One is the nonresonance point, which means no scattering wave from side branches; i.e., the frequency of incident wave $\omega = 0$. The other type of singular points stems from the destructive interference of multiple backscattering from the resonant units. For the former singular point, it always keeps at the origin for different setups of near-field coupling $\kappa$ and dimerized parameter $\Delta$. For the latter, however, the singular point moves in the parameters space composed of $\kappa$ and $\Delta$, which induces the band inversion when the singular point shifts from one pass band to another one.

The band inversion leads to contributing $\pi$ (or $-\pi$) to the Zak phase of two adjacent pass bands. It has been also argued that two kinds of single negative materials are appropriate to describe the trivial and nontrivial topological materials. The single negative materials are defined as $\varepsilon_{\mathrm{eff}}\mu_{\mathrm{eff}} < 0$, where $\varepsilon_{\mathrm{eff}}$ and $\mu_{\mathrm{eff}}$ are the effective relative permittivity and relative permeability. Concretely, the materials satisfying the conditions $\varepsilon_{\mathrm{eff}} < 0$ and $\mu_{\mathrm{eff}} > 0$ are $\varepsilon_{\mathrm{eff}}$-negative materials (ENG), while the ones satisfying $\varepsilon_{\mathrm{eff}} > 0$ and $\mu_{\mathrm{eff}} < 0$ are $\mu_{\mathrm{eff}}$-negative materials (MNG) [55–58]. $\varepsilon_{\mathrm{eff}}$ and $\mu_{\mathrm{eff}}$ of the studied 1D dimerized chain within the band gaps can be retrieved by using the standard method of the retrieval of the effective permittivity and permeability of metamaterials from the reflection and transmission coefficients [55,59], as shown in Fig. 4 with red dots and orange rhombus, respectively (see Appendix B). For the considered system above, the chains are, respectively, MNG and ENG in G2 for $\kappa = 0$ and $\kappa = -0.137\omega_0$ [see Figs. 4(a) and 4(f)]. The change of topological properties in G2 is consistent with the results of the band inversion analysis. When the EM wave is incident from the vacuum to a semi-infinite 1D dimerized chain, the reflection phase is positive for ENG and negative for MNG. These theoretical results provide more evidences to classify PTIs.

It should be mentioned that all band gaps are direct band gaps for the previously studied 1D dimerized chains with either far-field or near-field coupling only. Figure 4(a) shows an example of far-field coupling PTIs, where the momenta of the bottom of the upper band and the top of the lower band

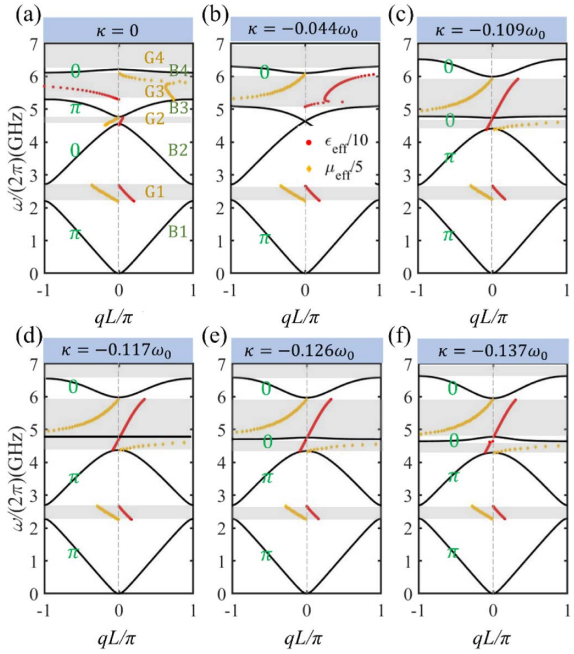


**Fig. 4.** Band structures of infinite 1D dimerized chain for a fixed dimerized parameter $\Delta = 0.165$, but different near-field coupling strengths. The gray shadows in (a) indicate band gaps marked as G1–G4, and the pass bands represented by the black lines are noted as B1–B4. The Zak phases for each band are marked. For other cases from (b) to (f), only the Zak phases are noted in the diagrams. The effective permittivity $\varepsilon_{\mathrm{eff}}$ and permeability $\mu_{\mathrm{eff}}$ for the band gaps are plotted. The materials with $\varepsilon_{\mathrm{eff}} < 0$ are the epsilon-negative materials (ENG) while the materials with $\mu_{\mathrm{eff}} < 0$ are mu-negative materials (MNG). ENG and MNG own different topological properties.

are always the same [47]. This situation has changed with the introduction of hybrid coupling. It has been shown in Figs. 4(b)–4(f) that an indirect band gap appears in the band diagram for the hybrid-coupling PTIs. For example, the gap G3 becomes an indirect gap when the near-field coupling is small ($\kappa = -0.109\omega_0$), as shown in Fig. 4(c). More interestingly, the dispersion of some bands (e.g., B1 and B2) seems unaffected by near-field coupling, whereas the dispersion of some other bands (e.g., B3 and B4) could be modified strongly with the increase of the near-field coupling strength [Figs. 4(a)–4(f)]. Comparing Fig. 4(e) with Fig. 4(c), it is obvious that the effective mass of photon at Γ point ($q = 0$) for B3 changes from positive to negative. It is worth noting that in Fig. 4(d), B3 becomes a flat band with a critical near-field coupling of $\kappa = -0.117\omega_0$, at which the two adjacent unit cells act as two perfectly reflecting mirrors at the flat band frequency. Thus, the waves can be completely localized between two unit cells. This behavior comes from the fact that the mechanisms of band generation for near-field coupling and far-field coupling are different. In the near-field model, the number of the bands is relevant to the number of the resonator sites in a unit cell, and band widths are dependent on the near-field coupling strength. For the far-field coupling case, however, the origination of the band gaps is caused by the destructive interference of multiple scattering; thus, we have infinite bands for the far-field coupling model due to periodic scattering. This is the reason why only limited bands, whose frequencies are near the resonance frequency, are modulated by the near-field coupling. The band dominated by the near-field coupling [B3 in Fig. 4(e)] shows distinguished dispersion relation compared to the band dominated by far-field coupling [B3 in Fig. 4(a)]. Such competition between far-field coupling and near-field coupling in the unit cell is absent in purely far-field coupling or near-field coupling systems. This unique characteristic may have applications in slow light photonic devices, as well as a nonlinear multiphoton process.

For a clearer insight into the effects of joint modulation of near-field and far-field couplings on the topological properties, the Zak phase diagram of the second pass band in the parameters space composed of $\kappa$ and $\Delta$ is plotted in Fig. 5. The first band gap is closed for certain $\kappa$ and $\Delta$ along the black dashed line and the second band gap is closed for $\kappa$ and $\Delta$ along the white lines. The diagram is divided into four regions due to the competition of near-field and far-field coupling and the relevant Zak phases are noted in Fig. 5. The Zak phase diagram is available for designing the 1D dimerized chain with specific topological properties.

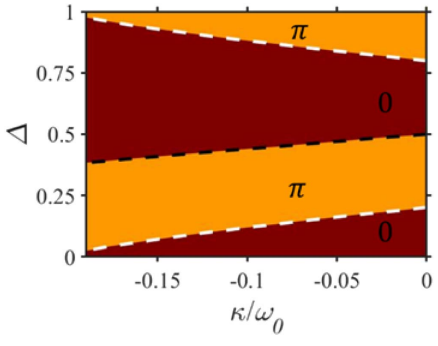


**Fig. 5.** Zak phase diagram of the second band under the joint modulation of near-field coupling $\kappa$ and the far-field coupling (dimerized parameter $\Delta$). The first band gap is closed for the $\kappa$ and $\Delta$ indicated by the black dashed line while the second band gap is closed for the $\kappa$ and $\Delta$ represented by the two white dashed lines.

## 4. EXPERIMENTAL DEMONSTRATION OF TOPOLOGICAL INTERFACE STATE WITH HYBRID COUPLING PTIS

Microwave experiments based on microstrip transmission line are conducted to demonstrate the hybrid-coupling-induced topological transition by measuring the reflection or transmission coefficients of the samples. The topologically distinguished two chains are composed of five unit cells with $\kappa = 0$ and $\kappa = -0.12\omega_0$, respectively (see Appendix C). The samples are fabricated on a 0.787 mm thick Rogers RT 5880 substrate (relative permittivity $\varepsilon_r = 2.2$) using printed-circuit-board technology [60], as shown in Fig. 6(a). We take the same width of side branch $h = 0.2$ mm, the same total length of side branch $l = 11.5$ mm (which determines the resonance frequency of the bare scatter), the same length of unit cell $L = 40$ mm, and the same dimerized parameter $\Delta = 0.165$ for the two samples. The intracell near-field coupling in hybrid PTI (sample II) is realized by bending the side branches toward each other in the same unit cell, where the gap $g = 0.2$ mm and the coupling length of the side branches $l_1 = 2.8$ mm.

We can theoretically calculate the reflection coefficient of the EM wave incident to the quasi-1D chain to compare it with the experimental results. The transfer matrix of a unit cell in the EM system is noted in Eq. (4). For five unit cells, the total transfer matrix $T^{(5)} = T^5$. The transmission and reflection coefficients are expressed in terms of the total transfer-matrix elements as $t = 1/T_{22}^{(5)}$ and $r = -T_{21}^{(5)}/T_{22}^{(5)}$.

The experimental and theoretical results of the reflection coefficients are shown in Fig. 6. The reflection spectra for sample I and sample II in Fig. 6(a) are plotted in Figs. 6(b) and 6(c), respectively. Three band gaps with high reflectivity represented by the gray area are shown in Figs. 6(b) and 6(c). The calculation results (black lines) of reflection amplitude agree well with the measurements (red dots). For the 2nd band gaps (G2), the reflection phases of the two samples are with opposite signs. The different sign of reflection phases for the 2nd band gaps indicates the topological transition induced by hybrid coupling in this 1D structure.

To further verify the different topological properties of these two dimerized chains, the topological interface state in sample III [see Fig. 6(a)] is investigated. The sample III is composed by two paired chains with a total length of 240 mm. According to surface bulk correspondence, there will be an interface mode emerging in the original gap G2 because of the opposite signs of the reflection phase. As shown in Fig. 6(d), a reflection valley indeed appears in the gap G2 region for the sample III in both calculated and measured reflection spectra. Moreover, the measured and simulated (CST MICROWAVE STUDIO) electric field distribution (in the backbone waveguide) at this reflection valley frequency ($f = 4.53$ GHz) is given in Fig. 6(e). Field enhancement at the interface ($x = 120$ mm) is observed.

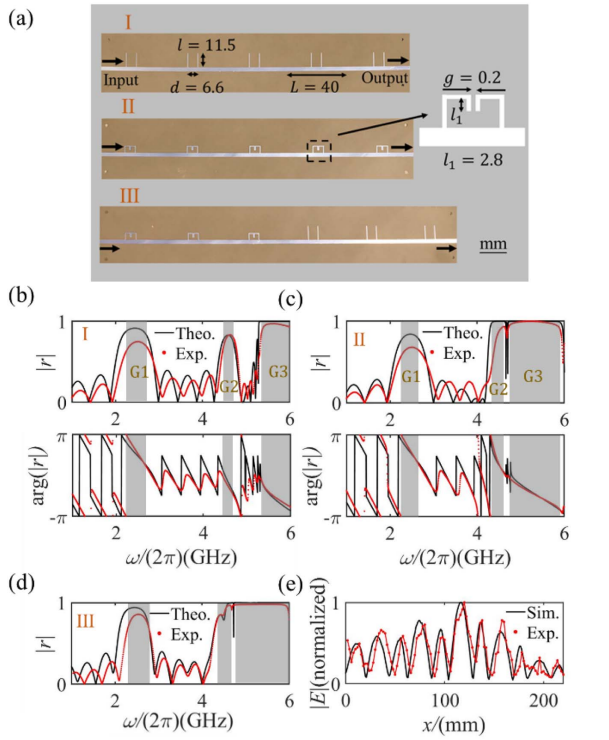


**Fig. 6.** (a) Three samples of 1D chain for (I) dimerized parameter $\Delta = 0.165$, near-field coupling $\kappa = 0$, (II) dimerized parameter $\Delta = 0.165$, near-field coupling $\kappa = -0.12\omega_0$, and (III) pairing of two aforementioned samples to demonstrate the topological interface state. The samples are fabricated on the Rogers RT 5880 double-side copper-clad board. The reflectivity and reflection phases for sample I and sample II are experimentally and theoretically shown in (b) and (c), respectively. The gray shadows indicate the band gaps. The reflection for the sample III is shown in (d), where the shadows are band gaps. There is a small valley only in the second band gap, which indicates the existence of an interface state. The electric field amplitude distribution of the interface state is measured and compared to the simulation results in (e).

The maximum electric field strength at the interface indicates that it is a topological interface mode.

## 5. CONCLUSION

In summary, we theoretically and experimentally investigate the topological properties of a dimerized 1D chain modulated by hybrid coupling. The introduced intracell near-field coupling in a far-field coupling dimerized chain can induce band inversion without tuning the dimerized parameter. Zak phases in this hybrid coupling model for different near-field couplings are investigated in detail. The interface mode is realized by pairing two dimerized chains with opposite reflection phases in the second band gaps to further confirm the topological phase transition. In addition, we notice that there are indirect band gaps in the hybrid coupling PTIs, and the near-field coupling only modulates the dispersion of the bands around the scatter resonance frequency. A flat band can be achieved by properly choosing the coupling parameters. The unit, which is near-field and far-field coupled to the other unit, is an analogue to the giant atom with multiple coupling channels in a quantum-waveguide system [61–63]. Hence, our model may provide a potential platform to study the interplay between giant atoms and topology. The results in our paper can be extended to a 2D case and even higher dimension.

## APPENDIX A: CALCULATION OF THE REFLECTION COEFFICIENT FOR THE SEMI-INFINITE 1D CHAIN

In this appendix, the calculation of the reflection coefficient for the semi-infinite dimerized 1D chain is shown. The transfer matrix related to the incoming wave and outcoming wave for the $n$th unit cell is given in the main text by $\begin{pmatrix} S^+_{n,L} \\ S^-_{n,L} \end{pmatrix} = T \begin{pmatrix} S^-_{n,R} \\ S^+_{n,R} \end{pmatrix}$. The elements in $T$ can be obtained from Eq. (4). In another definition, the transfer matrix is defined by

$$\begin{pmatrix} E_{n+1} \\ H_{n+1} \end{pmatrix} = M \begin{pmatrix} E_n \\ H_n \end{pmatrix}, \tag{A1}$$

which relates the electric and magnetic fields at two sides of the unit cell. The two transfer matrixes can linearly transform to each other in the form

$$M = PTP^{-1}, \tag{A2}$$

where $P = \begin{pmatrix} 1 & 1 \\ 1/Z_0 & -1/Z_0 \end{pmatrix}$ and $Z_0$ is the characteristic impedance of the microstrip transmission line. Here, we have $Z_0 = 50\ \Omega$. The impedance boundary condition requires that in the periodic structure, the impedance at all interfaces between unit cells should be the same, and we have

$$\frac{E_{n+1}}{H_{n+1}} = \frac{E_n}{H_n} = Z. \tag{A3}$$

From Eqs. (A2) and (A3), the solution for $Z$ is

$$Z = \frac{M_{11} - M_{22} \pm \sqrt{(M_{11} - M_{22})^2 + 4M_{21}M_{12}}}{2M_{21}}. \tag{A4}$$

As our system is passive, the real part of impedance $Z$ must be greater than zero. The reflection coefficient can thus be obtained by

$$r = \frac{Z - Z_0}{Z + Z_0}. \tag{A5}$$

## APPENDIX B: DETERMINATION OF EFFECTIVE PERMITTIVITY AND PERMEABILITY OF THE 1D PHOTONICS METAMATERIALS

In this appendix, we show that the effective relative permittivity ($\varepsilon_{\text{eff}}$) and relative permeability ($\mu_{\text{eff}}$) are determined from the reflection and transmission coefficients of a single unit cell. $\varepsilon_{\text{eff}}$ and $\mu_{\text{eff}}$ are related to the normalized impedance $Z$ and refractive index $n$ by $\varepsilon_{\text{eff}} = n/Z$ and $\mu_{\text{eff}} = nZ$; therefore, we can obtain the values of $\varepsilon_{\text{eff}}$ and $\mu_{\text{eff}}$ by retrieving $Z$ and $n$. Next, we show how to calculate $Z$ and $n$ from reflection and transmission coefficients.

For a 1D metamaterial with length $L$, the transmission coefficient is related to $Z$ and $n$ by

$$t^{-1} = \left[\cos(nkL) - \frac{i}{2}\left(Z + \frac{1}{Z}\right)\sin(nkL)\right]e^{ikL}, \tag{B1}$$

where $k = \omega/c$ is wavenumber of the incident wave. On the other hand, the reflection coefficient $r$ is also related to $Z$ and $n$ by

$$\frac{r}{t'} = -\frac{i}{2}\left(Z - \frac{1}{Z}\right)\sin(nkL). \tag{B2}$$

Here, $t' = te^{ikL}$. $Z$ and $n$ can be found by inverting Eqs. (B1) and (B2). The expression of $Z$ is given as

$$Z = \pm\sqrt{\frac{(1+r)^2 - t'^2}{(1-r)^2 - t'^2}}. \tag{B3}$$

For the passive materials, the requirement that $\mathrm{Re}(Z) > 0$ should guarantee the choice of $Z$. For refractive index $n$, we have the imaginary and real parts

$$\mathrm{Im}(n) = \pm\mathrm{Im}\left\{\frac{\arccos\left\{\frac{1}{2t'}[1-(r^2-t'^2)]\right\}}{kL}\right\}, \tag{B4}$$

$$\mathrm{Re}(n) = \pm\mathrm{Re}\left\{\frac{\arccos\left\{\frac{1}{2t'}[1-(r^2-t'^2)]\right\}}{kL}\right\} + \frac{2\pi m}{kL}, \tag{B5}$$

where $m$ is an integer. Similarly, the passive materials require $\mathrm{Im}(n) > 0$, which leads to the definite results of $\mathrm{Im}(n)$ and $\mathrm{Re}(n)$. In our system, $L$ is smaller than the wavelength in the studied frequency band. The cumulative phase when the EM wave propagates through a unit cell does not surpass $2\pi$ and therefore we take $m = 0$ in our calculation.

## APPENDIX C: DETERMINATION OF THE PARAMETERS THROUGH CURVE FITTINGS

In this appendix, the fitted parameters of far-field coupling $\gamma$, resonant frequency $f_0$ of the resonant sites, and near-field coupling $\kappa$ are obtained by curve fittings.

First, we show how to obtain the values of far-field coupling $\gamma$ and resonant frequency $f_0$. For a side resonant branch excited by the EM wave from Port1 through the transmission channel as shown in Fig. 7(a), the dynamics equation of the resonant mode ($\tilde{a}_1 = a_1 e^{i\omega t}$) at the side branch can be written as

$$\dot{\tilde{a}}_1 = (i\omega_0 - \gamma - \Gamma)\tilde{a}_1 + i\sqrt{\gamma}e^{-ikL/2}\tilde{S}_L^+, \tag{C1}$$

where $\omega_0 = 2\pi f_0$ and $\Gamma$ is the intrinsic loss of the side branch. The parameters in Fig. 7(a) are $L = 40$ mm, $h = 0.2$ mm, and $l = 11.5$ mm. The reflection at Port1 reads

$$r_1 = i\sqrt{\gamma}e^{-ikL/2}a_1/S_L^+. \tag{C2}$$

By fitting the reflectivity obtained from the simulation with Eq. (C2), where $\gamma$, $f_0$, and $\Gamma$ are three parameters to be determined [shown in Fig. 7(b)], we have $\gamma = 4.19$ GHz, $f_0 = 5.83$ GHz, and $\Gamma = 0.023$ GHz. The intrinsic loss $\Gamma$ is negligible compared to $\gamma$. Thus, the effect of intrinsic loss is not considered in the main text.

Next the same method is used to find out the value of near-field coupling $\kappa$. The schematic of a unit cell with near-field coupling and far-field coupling existing simultaneously between two resonant modes is given in Fig. 7(c). Here, $d = 6.6$ mm corresponding to $\Delta = 0.165$, $g = 0.2$ mm, and $l_1 = 2.8$ mm. Using Eq. (6) to fit the reflectivity from simulation, we have $\kappa = -4.4$ GHz.

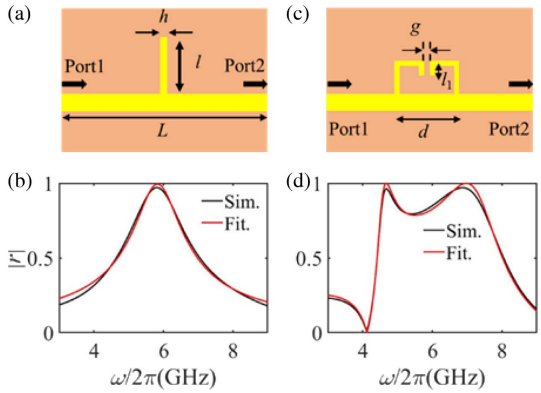


**Fig. 7.** (a) Schematic of a side resonant branch excited by the EM waves from Port1 and (b) the simulation (black line) and fitted reflectivity (red line) of the EM wave. (c) Near-field coupling and far-field coupling coexist between two resonant branches in the same unit cell and (d) the simulation (black line) and fitted reflectivity (red line) when the EM wave is incident from the left.

**Funding.** National Key Research and Development Program of China (2020YFA0211400, 2020YFA0211402); National Natural Science Foundation of China (91850206, 11974261, 61621001, 12104105); Shanghai Pujiang Program (21PJ1411400); Fundamental Research Funds for the Central Universities.

**Disclosures.** The authors declare no conflicts of interest.

**Data Availability.** Data underlying the results presented in this paper are not publicly available at this time but may be obtained from the authors upon reasonable request.

## REFERENCES

1. C. L. Kane and E. J. Mele, "Quantum spin Hall effect in graphene," Phys. Rev. Lett. **95**, 226801 (2005).
2. N. H. Lindner, G. Refael, and V. Galitski, "Floquet topological insulator in semiconductor quantum wells," Nat. Phys. **7**, 490–495 (2011).
3. D. J. Thouless, M. Kohmoto, M. P. Nightingale, and M. den Nijs, "Quantized Hall conductance in a two-dimensional periodic potential," Phys. Rev. Lett. **49**, 405–408 (1982).
4. X. G. Wen, "Topological orders and edge excitations in fractional quantum Hall states," Adv. Phys. **44**, 405–473 (1995).
5. Z. Wang, Y. D. Chong, J. D. Joannopoulos, and M. Soljačić, "Reflection-free one-way edge modes in a gyromagnetic photonic crystal," Phys. Rev. Lett. **100**, 013905 (2008).
6. H. Zhao, X. Qiao, T. Wu, B. Midya, S. Longhi, and L. Feng, "Non-Hermitian topological light steering," Science **365**, 1163–1166 (2019).
7. C. Lu, C. Wang, M. Xiao, Z. Q. Zhang, and C. T. Chan, "Topological rainbow concentrator based on synthetic dimension," Phys. Rev. Lett. **126**, 113902 (2021).
8. H. Zhang, L. Qian, C. Wang, C.-Y. Ji, Y. Liu, J. Chen, and C. Lu, "Topological rainbow based on graded topological photonic crystals," Opt. Lett. **46**, 1237–1240 (2021).
9. M. Atala, M. Aidelsburger, J. T. Barreiro, D. Abanin, T. Kitagawa, E. Demler, and I. Bloch, "Direct measurement of the Zak phase in topological Bloch bands," Nat. Phys. **9**, 795–800 (2013).
10. F. Gao, Z. Gao, X. Shi, Z. Yang, X. Lin, H. Xu, J. D. Joannopoulos, M. Soljačić, H. Chen, L. Lu, Y. Chong, and B. Zhang, "Probing topological protection using a designer surface plasmon structure," Nat. Commun. **7**, 11619 (2016).

11. Z. Gao, Z. Yang, F. Gao, H. Xue, Y. Yang, J. Dong, and B. Zhang, "Valley surface-wave photonic crystal and its bulk/edge transport," Phys. Rev. B **96**, 201402 (2017).
12. A. B. Khanikaev, S. H. Mousavi, W.-K. Tse, M. Kargarian, A. H. MacDonald, and G. Shvets, "Photonic topological insulators," Nat. Mater. **12**, 233–239 (2013).
13. M. Kremer, I. Petrides, E. Meyer, M. Heinrich, O. Zilberberg, and A. Szameit, "A square-root topological insulator with non-quantized indices realized with photonic Aharonov-Bohm cages," Nat. Commun. **11**, 907 (2020).
14. J. Ma, J.-W. Rhim, L. Tang, S. Xia, H. Wang, X. Zheng, S. Xia, D. Song, Y. Hu, Y. Li, B.-J. Yang, D. Leykam, and Z. Chen, "Direct observation of flatband loop states arising from nontrivial real-space topology," Phys. Rev. Lett. **124**, 183901 (2020).
15. M. C. Rechtsman, Y. Plotnik, J. M. Zeuner, D. Song, Z. Chen, A. Szameit, and M. Segev, "Topological creation and destruction of edge states in photonic graphene," Phys. Rev. Lett. **111**, 103901 (2013).
16. J. Song, F. Yang, Z. Guo, X. Wu, K. Zhu, J. Jiang, Y. Sun, Y. Li, H. Jiang, and H. Chen, "Wireless power transfer via topological modes in dimer chains," Phys. Rev. Appl. **15**, 014009 (2021).
17. S. Xia, D. Song, N. Wang, X. Liu, J. Ma, L. Tang, H. Buljan, and Z. Chen, "Topological phenomena demonstrated in photorefractive photonic lattices," Opt. Mater. Express **11**, 1292–1312 (2021).
18. M. Xiao, Z. Q. Zhang, and C. T. Chan, "Surface impedance and bulk band geometric phases in one-dimensional systems," Phys. Rev. X **4**, 021017 (2014).
19. M. Li, D. Zhirihin, M. Gorlach, X. Ni, D. Filonov, A. Slobozhanyuk, A. Alù, and A. B. Khanikaev, "Higher-order topological states in photonic Kagome crystals with long-range interactions," Nat. Photonics **14**, 89–94 (2020).
20. S. Liu, S. Ma, Q. Zhang, L. Zhang, C. Yang, O. You, W. Gao, Y. Xiang, T. J. Cui, and S. Zhang, "Octupole corner state in a three-dimensional topological circuit," Light Sci. Appl. **9**, 145 (2020).
21. B.-Y. Xie, G.-X. Su, H.-F. Wang, H. Su, X.-P. Shen, P. Zhan, M.-H. Lu, Z.-L. Wang, and Y.-F. Chen, "Visualization of higher-order topological insulating phases in two-dimensional dielectric photonic crystals," Phys. Rev. Lett. **122**, 233903 (2019).
22. Y. Yang, Z. Gao, H. Xue, L. Zhang, M. He, Z. Yang, R. Singh, Y. Chong, B. Zhang, and H. Chen, "Realization of a three-dimensional photonic topological insulator," Nature **565**, 622–626 (2019).
23. S. Weimann, M. Kremer, Y. Plotnik, Y. Lumer, S. Nolte, K. G. Makris, M. Segev, M. C. Rechtsman, and A. J. N. Szameit, "Topologically protected bound states in photonic parity–time-symmetric crystals," Nat. Mater. **16**, 433–438 (2017).
24. D.-W. Zhang, L.-Z. Tang, L.-J. Lang, H. Yan, and S.-L. Zhu, "Non-Hermitian topological Anderson insulators," Sci. China: Phys., Mech. Astron. **63**, 267062 (2020).
25. M. Guo, S. Xia, N. Wang, D. Song, Z. Chen, and J. Yang, "Weakly nonlinear topological gap solitons in Su–Schrieffer–Heeger photonic lattices," Opt. Lett. **45**, 6466–6469 (2020).
26. M. C. Rechtsman, J. M. Zeuner, Y. Plotnik, Y. Lumer, D. Podolsky, F. Dreisow, S. Nolte, M. Segev, and A. J. N. Szameit, "Photonic Floquet topological insulators," Nature **496**, 196–200 (2013).
27. F. D. M. Haldane and S. Raghu, "Possible realization of directional optical waveguides in photonic crystals with broken time-reversal symmetry," Phys. Rev. Lett. **100**, 013904 (2008).
28. Z. Wang, Y. Chong, J. D. Joannopoulos, and M. Soljačić, "Observation of unidirectional backscattering-immune topological electromagnetic states," Nature **461**, 772–775 (2009).
29. M. Hafezi, E. A. Demler, M. D. Lukin, and J. M. Taylor, "Robust optical delay lines with topological protection," Nat. Phys. **7**, 907–912 (2011).
30. K. Lai, T. Ma, X. Bo, S. Anlage, and G. Shvets, "Experimental realization of a reflections-free compact delay line based on a photonic topological insulator," Sci. Rep. **6**, 28453 (2016).
31. S. A. Mann, D. L. Sounas, and A. Alù, "Broadband delay lines and nonreciprocal resonances in unidirectional waveguides," Phys. Rev. B **100**, 020303 (2019).
32. K. Fang, J. Luo, A. Metelmann, M. H. Matheny, F. Marquardt, A. A. Clerk, and O. Painter, "Generalized non-reciprocity in an optomechanical circuit via synthetic magnetism and reservoir engineering," Nat. Phys. **13**, 465–471 (2017).
33. W. Gao, X. Hu, C. Li, J. Yang, Z. Chai, J. Xie, and Q. Gong, "Fano-resonance in one-dimensional topological photonic crystal heterostructure," Opt. Express **26**, 8634–8644 (2018).
34. X. Wang, Y. Liang, L. Wu, J. Guo, X. Dai, and Y. Xiang, "Multi-channel perfect absorber based on a one-dimensional topological photonic crystal heterostructure with graphene," Opt. Lett. **43**, 4256–4259 (2018).
35. S. Longhi, "Zak phase of photons in optical waveguide lattices," Opt. Lett. **38**, 3716–3719 (2013).
36. J. Lu, L. He, Z. Addison, E. J. Mele, and B. Zhen, "Floquet topological phases in one-dimensional nonlinear photonic crystals," Phys. Rev. Lett. **126**, 113901 (2021).
37. A. Poddubny, A. Miroshnichenko, A. Slobozhanyuk, and Y. Kivshar, "Topological Majorana states in zigzag chains of plasmonic nanoparticles," ACS Photon. **1**, 101–105 (2014).
38. C. Schmidt, A. Palatnik, M. Sudzius, S. Meister, and K. Leo, "Coupled topological interface states," Phys. Rev. B **103**, 085412 (2021).
39. A. P. Slobozhanyuk, A. N. Poddubny, A. E. Miroshnichenko, P. A. Belov, and Y. S. Kivshar, "Subwavelength topological edge states in optically resonant dielectric structures," Phys. Rev. Lett. **114**, 123901 (2015).
40. Q. Wang, M. Xiao, H. Liu, S. Zhu, and C. T. Chan, "Measurement of the Zak phase of photonic bands through the interface states of a metasurface/photonic crystal," Phys. Rev. B **93**, 041415 (2016).
41. N. Malkova, I. Hromada, X. Wang, G. Bryant, and Z. Chen, "Observation of optical Shockley-like surface states in photonic superlattices," Opt. Lett. **34**, 1633–1635 (2009).
42. N. Malkova, I. Hromada, X. Wang, G. Bryant, and Z. Chen, "Transition between Tamm-like and Shockley-like surface states in optically induced photonic superlattices," Phys. Rev. A **80**, 043806 (2009).
43. M. Di Liberto, A. Recati, I. Carusotto, and C. Menotti, "Two-body physics in the Su–Schrieffer–Heeger model," Phys. Rev. A **94**, 062704 (2016).
44. G. Go, I.-S. Hong, S.-W. Lee, S. K. Kim, and K.-J. Lee, "Realization of Su-Schrieffer-Heeger states based on metamaterials of magnetic solitons," Phys. Rev. B **101**, 134423 (2020).
45. L.-J. Lang, Y. Wang, H. Wang, and Y. D. Chong, "Effects of non-Hermiticity on Su–Schrieffer–Heeger defect states," Phys. Rev. B **98**, 094307 (2018).
46. N. Kaina and R. Fleury, "Hermitian formulation of multiple scattering induced topological phases in metamaterial crystals," Phys. Rev. B **102**, 134303 (2020).
47. W. Zhu, Y.-Q. Ding, J. Ren, Y. Sun, Y. Li, H. Jiang, and H. Chen, "Zak phase and band inversion in dimerized one-dimensional locally resonant metamaterials," Phys. Rev. B **97**, 195307 (2018).
48. C. W. Hsu, B. Zhen, A. D. Stone, J. D. Joannopoulos, and M. Soljačić, "Bound states in the continuum," Nat. Rev. Mater. **1**, 16048 (2016).
49. J. W. Rao, Y. T. Zhao, Y. S. Gui, X. L. Fan, D. S. Xue, and C. M. Hu, "Controlling microwaves in non-Hermitian metamaterials," Phys. Rev. Appl. **15**, L021003 (2021).
50. E. Lamothe, G. Leveque, and O. J. F. Martin, "Optical forces in coupled plasmonic nanosystems: near field and far field interaction regimes," Opt. Express **15**, 9631–9644 (2007).
51. B. Gallinet and O. J. F. Martin, "Relation between near-field and far-field properties of plasmonic Fano resonances," Opt. Express **19**, 22167–22175 (2011).
52. S. H. Fan, W. Suh, and J. D. Joannopoulos, "Temporal coupled-mode theory for the Fano resonance in optical resonators," J. Opt. Soc. Am. A **20**, 569–572 (2003).
53. W. Tan, Y. Sun, Z.-G. Wang, and H. Chen, "Manipulating electromagnetic responses of metal wires at the deep subwavelength scale via both near- and far-field couplings," Appl. Phys. Lett. **104**, 091107 (2014).
54. J. Zak, "Berry's phase for energy-bands in solids," Phys. Rev. Lett. **62**, 2747–2750 (1989).
55. J. Guo, Y. Sun, Y. Zhang, H. Li, H. Jiang, and H. Chen, "Experimental investigation of interface states in photonic crystal heterostructures," Phys. Rev. E **78**, 026607 (2008).

56. Q. Huang, Z. Guo, J. Feng, C. Yu, H. Jiang, Z. Zhang, Z. Wang, and H. Chen, "Observation of a topological edge state in the X-ray band," Laser Photon. Rev. **13**, 1800339 (2019).
57. X. Shi, C. Xue, H. Jiang, and H. Chen, "Topological description for gaps of one-dimensional symmetric all-dielectric photonic crystals," Opt. Express **24**, 18580–18591 (2016).
58. W. Tan, Y. Sun, H. Chen, and S.-Q. Shen, "Photonic simulation of topological excitations in metamaterials," Sci. Rep. **4**, 3842 (2014).
59. D. R. Smith, S. Schultz, P. Markos, and C. M. Soukoulis, "Determination of effective permittivity and permeability of metamaterials from reflection and transmission coefficients," Phys. Rev. B **65**, 195104 (2002).
60. C. F. Coombs, Jr., *Printed Circuits Handbook* (McGraw-Hill Education, 2008).
61. L. Guo, A. F. Kockum, F. Marquardt, and G. Johansson, "Oscillating bound states for a giant atom," Phys. Rev. Res. **2**, 043014 (2020).
62. M. V. Gustafsson, T. Aref, A. F. Kockum, M. K. Ekstrom, G. Johansson, and P. Delsing, "Propagating phonons coupled to an artificial atom," Science **346**, 207–211 (2014).
63. A. M. Vadiraj, A. Ask, T. G. McConkey, I. Nsanzineza, C. W. S. Chang, A. F. Kockum, and C. M. Wilson, "Engineering the level structure of a giant artificial atom in waveguide quantum electrodynamics," Phys. Rev. A **103**, 023710 (2021).